# Vigorous atmospheric motions in the red supergiant supernova progenitor Antares

K. Ohnaka[1], G. Weigelt[2] & K.-H. Hofmann[2]

1. Instituto de Astronomía, Universidad Católica del Norte, Avenida Angamos 0610, Antofagasta, Chile
2. Max-Planck-Institut für Radioastronomie, Auf dem Hügel 69, 53121 Bonn, Germany

**Red supergiants represent a late stage of the evolution of stars more massive than about 9 solar masses. At this evolutionary stage, massive stars develop complex, multi-component atmospheres. Bright spots were detected in the atmosphere of red supergiants by interferometric imaging[1–5]. Above the photosphere, the molecular outer atmosphere extends up to about two stellar radii[6–14]. Furthermore, the hot chromosphere (5,000–8,000 K) and cool gas (<3,500 K) are coexisting within ∼3 stellar radii[15–18]. The dynamics of the complex atmosphere have been probed by ultraviolet and optical spectroscopy[19–22]. However, the most direct, unambiguous approach is to measure the velocity at each position over the image of stars as in observations of the Sun. Here we report mapping of the velocity field over the surface and atmosphere of the prototypical red supergiant Antares. The two-dimensional velocity field map obtained from our near-infrared spectro-interferometric imaging reveals vigorous upwelling and downdrafting motions of several huge gas clumps at velocities ranging from about $-20$ to $+20$ km s$^{-1}$ in the atmosphere extending out to ∼1.7 stellar radii. Convection alone cannot explain the observed turbulent motions and atmospheric extension, suggesting the operation of a yet-to-be identified process in the extended atmosphere.**

Antares is a well-studied, close red supergiant (RSG) at a distance of $170^{+35}_{-25}$ pc (based on the parallax of $5.89 \pm 1.00$ milliarcsecond = mas, ref. 23). We observed Antares with the Very Large Telescope Interferometer (VLTI) of the European Southern Observatory (ESO) located on Cerro Paranal in Chile to directly see the gas motions in the atmosphere. The near-infrared VLTI instrument AMBER[24] allowed us to record spectrally dispersed interferograms across CO lines between 2.28 and 2.31 $\mu$m with a spectral resolution of 12,000. This is sufficient to have approximately 10 wavelength channels across each CO line and is crucial for directly seeing the dynamics of the spatially resolved atmosphere of the star. We obtained VLTI/AMBER data covering baselines from 4.6 to 82 m and reconstructed images of Antares at 311 wavelength channels across the observed wavelength range (see Methods).

Figure 1 shows the images of Antares reconstructed at eight different wavelength channels. Thanks to a superb spatial resolution of $5.1 \times 5.4$ mas, several structures are well resolved with unprecedented spatial and velocity accuracy. The spatial resolution is about seven times finer than the star's angular diameter of $37.61 \pm 0.12$ mas in the continuum (see Methods) and nearly 12 times finer than the extension of the atmosphere. The continuum images (Figs. 1a and 1e) show a nearly smooth surface with a weak, large spot at the centre with an intensity contrast of 3–4% (see Methods for the reliability of image reconstruction). In marked contrast, the images in the CO band head (Figs. 1b, 1c, and 1d) as well as those in the CO lines (Figs. 1f, 1g, and 1h) clearly reveal two large spots with a contrast of $\sim$20% and an irregularly shaped atmosphere extending out to $\sim$1.7 stellar radii ($\approx$32 mas). These spots may represent regions with lower CO densities, through which the emission from the lower, warmer layers can be seen.

The previous images of the spotty surface of RSGs were taken in the visible, where the strong TiO bands are present[1–3]. On the other hand, the image of the well-studied RSG Betelgeuse (similar to Antares) taken at 833 nm, which better represents the continuum, shows a featureless, limb-darkened disc[25]. The observations at longer wavelengths of 905 and 1290 nm show that the spots are weak or absent at these wavelengths, which can be explained by smaller TiO opacity[3] at longer wavelengths. The images and modeling of interferometric data of RSGs at $\sim$1.6 $\mu$m show weak to moderate spots presumably due to a jumble of weak and moderate lines of CO and CN[4,5,26]. These results are consistent with our observations in that Antares shows a nearly smooth surface in the continuum, and the inhomogeneities appear in the CO lines that form in the upper layers of the atmosphere.

From the data cube of the images reconstructed at 311 wavelength channels, we extracted the spatially resolved spectrum at each position over the surface of the star and the extended atmosphere. Figure 2 shows the spatially resolved spectra (red lines) with a spectral resolution of 8,000 (see Methods) at the three representative positions A (on the stellar disc) and B and C (in the atmosphere), together with the spatially unresolved spectrum (i.e., the spectrum averaged over the entire image; black lines). On the one hand, as can be seen in Fig. 2b, the spatially resolved spectrum (red line) of the bright spot on the surface (position A) shows stronger absorption lines than the spatially unresolved spectrum. On the other hand, the spatially resolved spectra in the atmosphere (positions B and C) show the CO lines in prominent emission (Figs. 2d and 2f)—exactly as expected from the Kirchhoff's law.

A closer look at the spatially resolved line profiles reveals that the absorption lines at the position A (Fig. 2c, red line) is slightly blueshifted with respect to the spatially unresolved spectrum (Fig. 2c, black line), which means that the gas at this position A is upwelling. In Fig. 2e, the peaks of the CO emission lines at the position B are clearly blueshifted with respect to the absorption lines seen in the spatially unresolved spectrum, indicating that the gas at the position B is moving towards us. In contrast, the CO emission lines at the position C are redshifted with respect to the spatially unresolved spectrum (Fig. 2g), which means that the gas is moving away from us.

We measured the line-of-sight (LOS) gas velocity at each position over the stellar disc and atmosphere by calculating the cross-correlation between the spatially resolved and unresolved spectra. Figure 3 shows the two-dimensional velocity field map of Antares obtained in this manner (positive and negative velocities indicate the gas moving away from us and approaching towards us, respectively). We resolved the velocity field over the stellar disc that reveals upwelling and downdrafting at LOS velocities ranging from approximately $-20$ to $+10$ km s$^{-1}$ on a spatial scale of the radius of the star. The gas motions in the extended atmosphere are characterised by vigorous, inhomogeneous motions of several large clumps at LOS velocities ranging from $-10$ to $+20$ km s$^{-1}$. We note, however, that while the positive and negative LOS velocities observed over the stellar disc can be readily associated with downdrafting and upwelling motions, respectively, there is ambiguity for the clumps observed in the extended atmosphere (i.e, outside the limb of the stellar disc). For example, the clump in the northwest with an LOS velocity of 20 km s$^{-1}$ may be infalling on the observer's side of the system (i.e., in front of the plane perpendicular to the LOS and going through the star's centre) or outflowing on the far side of the star (i.e., behind the aforementioned plane).

These upwelling and downdrafting motions resemble convection on the surface of RSGs[27]. However, the observationally estimated density in the atmosphere is at least six orders of magnitude higher, and the atmospheric extension is much larger than predicted by the current convection models[13,28]. This suggests that convection alone cannot lift up the material to the observed radius of $\sim$1.7 stellar radii, and the CO lines originate in layers higher than the top of convective cells. This can explain the absence of a correlation between the images in the continuum (probing the convection-dominated deep layers) and those in the CO lines (probing the extended atmosphere).

Similar upward and downward motions are inferred in the chromosphere of Betelgeuse, but the velocity amplitude is much smaller, $\sim$5 km s$^{-1}$ (refs. 19, 20). The analysis of optical line profiles in a sample of RSGs (but not including Antares) suggests upward and downward velocities of up to 17 km s$^{-1}$ in the upper layers of the atmosphere[22]. The velocities are comparable to what we measured in Antares, although the authors of ref. 22 interpret the motions as originating from convection unlike our argument above. However, the interpretation of spectral lines obtained by spatially unresolved spectroscopy (i.e., averaged over the entire surface and atmosphere of a star) in terms of atmospheric motions can be ambiguous. For example, a different analysis[29] of the radial velocities of optical spectral lines of Antares suggests that the convective motions penetrate only the lower photosphere (in line with our argument above) and that the lines forming in the upper atmosphere show only weak atmospheric motions (distinct from our results).

Since convection alone cannot explain the density and extension of the atmosphere, some yet-to-be identified process should be in operation to make the atmosphere extended and give rise to the turbulent motions and also perhaps the mass loss. Given that we did not detect a systematic outflow within 1.7 stellar radii, the substantial acceleration of mass loss should take place beyond this radius. The next challenge remains to identify the driving mechanism responsible for the observed turbulent motions. Our technique to map out the velocity field over the surface and atmosphere of stars other than the Sun can be extended to different atomic and molecular lines forming at different atmospheric heights. Such tomographic velocity-resolved imaging will provide us with a three-dimensional picture of the dynamics of stellar atmospheres from deep layers to the outer atmosphere and help us identify the process behind the observed atmospheric motions.

1. Buscher, D. F., Haniff, C. A., Baldwin, J. E., & Warner, P. J. Detection of a bright feature on the surface of Betelgeuse. Mon. Not. R. Astron. Soc., **245**, 7-11 (1990)

2. Tuthill, P. G., Haniff, C. A., & Baldwin, J. E. Hotspots on late-type supergiants. Mon. Not. R. Astron. Soc., **285**, 529-539 (1997)

3. Young, J. S., et al. New views of Betelgeuse: multi-wavelength surface imaging and implications for models of hotspot generation. Mon. Not. R. Astron. Soc., **315**, 635-645 (2000)

4. Haubois, X. et al. Imaging the spotty surface of Betelgeuse in the H band. Astron. Astrophys., **508**, 923-932 (2009)

5. Baron, F., et al. CHARA/MIRC observations of two M supergiants in Perseus OB1: temperature, Baysian modeling, and compressed sensing imaging. Astrophys. J. **785**, 46 (2014)

6. Tsuji, T. Water on the early M supergiant stars $\alpha$ Orionis and $\mu$ Cephei. Astrophys. J., **538**, 801-807 (2000)

7. Tsuji, T. Water in emission in the Infrared Space Observatory spectrum of the early M supergiant star $\mu$ Cephei. Astrophys. J., **540**, L99-L102 (2000)

8. Perrin, G. et al. Interferometric observations of the supergiant stars $\alpha$ Orionis and $\alpha$ Herculis with FLUOR at IOTA. Astron. Astrophys., **418**, 675-685 (2004)

9. Ohnaka, K. Warm water vapor envelope in the supergiants $\alpha$ Ori and $\alpha$ Her and its effects on the apparent size from the near-infrared to the mid-infrared. Astron. Astrophys., **421**, 1149-1158 (2004)

10. Harper, G. M. et al. 2009, TEXES observations of M supergiants: dynamics and thermodynamics of wind acceleration. Astrophys. J., **701**, 1464-1483 (2009)

11. Ohnaka, K. et al. Spatially resolving the inhomogeneous structure of the dynamical atmosphere of Betelgeuse with VLTI/AMBER. Astron. Astrophys., **503**, 183-195 (2009)

12. Ohnaka, K. et al. Imaging the dynamical atmosphere of the red supergiant Betelgeuse in the CO first overtone lines with VLTI/AMBER. Astron. Astrophys., **529**, A163 (2011)

13. Ohnaka, K. et al. High spectral resolution imaging of the dynamical atmosphere of the red supergiant Antares in the CO first overtone lines with VLTI/AMBER. Astron. Astrophys., **555**, A24 (2013)

14. Montargès, M. et al. Properties of the CO and $H_2O$ MOLsphere of the red supergiant Betelgeuse from VLTI/AMBER observations. Astron. Astrophys., **572**, A17 (2014)

15. Gilliland, R. L. & Dupree, A. K. First image of the surface of a star with the Hubble Space Telescope. Astrophys. J., **463**, L29-L32 (1996)

16. Lim, J., Carilli, C. L., White, S. M., Beasley, A. J. & Marson, R. G. Large convection cells as the source of Betelgeuse's extended atmosphere. Nature, **392**, 575-577 (1998)

17. Harper, G. M. & Brown, A. Spatially resolved, semiempirical model for the extended atmosphere of $\alpha$ Orionis (M2 Iab). Astrophys. J., **551**, 1073-1098 (2001)

18. Harper, G. M. & Brown, A. Electron density and turbulence gradients within the extended atmosphere of the M supergiant Betelgeuse ($\alpha$ Orionis). Astrophys. J., **646**, 1179-1202 (2006)

19. Lobel, A. & Dupree, A. K. Modeling the variable chromosphere of $\alpha$ Orionis. Astrophys. J., **545**, 454-474 (2000)

20. Lobel, A. & Dupree, A. K. Spatially resolved STIS spectroscopy of $\alpha$ Orionis: evidence for nonradial chromospheric oscillation from detailed modeling. Astrophys. J., **558**, 815-829 (2001)

21. Gray, D. F. Mass motions in the photosphere of Betelgeuse. Astron. J., **135**, 1450-1458 (2008)

22. Josselin, E., & Plez, B. Atmospheric dynamics and the mass loss process in red supergiant stars. Astron. Astrophys., **469**, 671-680 (2007)

23. van Leeuwen, F. Validation of the new Hipparcos reduction. Astron. Astrophys., **474**, 653-664 (1997)

24. Petrov, R. et al. AMBER, the near-infrared spectro-interferometric three-telescope VLTI instrument. Astron. Astrophys., **464**, 1-12 (2007)

25. Burns, D. et al. The surface structure and limb-darkening profile of Betelgeuse. Mon. Not. R. Astron. Soc., **290**, L11-L16 (1997)

26. Montargès, M., et al. The close circumstellar environment of Betelgeuse IV. VLTI/PIONIER interferometric monitoring of the photosphere. Astron. Astrophys., **588**, A130 (2016)

27. Chiavassa, A., Freytag, B., Masseron, T. & Plez, B. Radiative hydrodynamics simulations of red supergiant stars. IV. Gray versus non-gray opacities. Astron. Astrophys., **535**, A22 (2011)

28. Arroyo-Torres, B. et al. What causes the large extensions of red supergiant atmospheres? Comparison of interferometric observations with 1D hydrostatic, 3D convection, and 1D pulsating model atmospheres. Astron. Astrophys., **575**, A50 (2015)

29. Gray, D. F., & Pugh, T. The third signature of granulation in bright-giant and supergiant stars. Astron. J., **143**, 92 (2012)

**Supplementary Information** is linked to the online version of the paper at www.nature.com/nature.

**Acknowledgements** We thank the ESO VLTI team for their support for our VLTI/AMBER observations. This work is based on AMBER observations made with the Very Large Telescope Interferometer of the European Southern Observatory (Program ID: 093.D-0468A/B). K.O. acknowledges the grant from the Universidad Católica del Norte.

**Author contributions** K.O. wrote the telescope proposal and the first paper manuscript, carried out the observations, data reduction, and image reconstruction, and worked on data interpretation. G.W. and K.-H.H. were co-authors on the telescope proposal and worked on data reduction and interpretation.

**Competing Interests** The authors declare that they have no competing financial interests.

**Author Information** Correspondence and requests for materials should be addressed to K.O.
(email: k1.ohnaka@gmail.com).

Figure 1: Reconstructed velocity-resolved images of Antares. The images reconstructed at four wavelength channels near the CO band head are shown in panels **a–d**, while those across one of the CO lines are shown in panels **e–h**. The images in the continuum (**a** and **e**) show the nearly smooth stellar disc. The images in the CO band head and the CO line (**c**, **d**, **f**, **g**, and **h**) reveal two bright spots on the stellar disc and the clumpy, extended atmosphere. The beam size ($5.1 \times 5.4$ mas) is shown in the lower right corner of each panel. North is up, east is to the left. **i–k:** Observed spectrum of Antares. Enlarged views of two wavelength ranges (marked with the rectangles in panel **j**) are shown in panels **i** and **k**. In these two panels, the wavelength channels of the images in panels **a–h** are marked with the corresponding alphabetic characters.

Figure 2: Spatially resolved spectra over the stellar disc and atmosphere of Antares. **a:** Image reconstructed at the centre of the CO line at 2.30665 $\mu$m (north is up, east is to the left). The beam size is shown in the lower right corner. The crosses mark the three positions at which the spatially resolved spectra shown in panels **b**–**g** were extracted. **b** and **c**: Spatially resolved spectrum obtained at the position A on the stellar disc. The red lines represent the (scaled) spatially resolved spectrum, while the black lines show the spatially unresolved spectrum (i.e., spectrum averaged over the entire image). Panel **b** shows a comparison for a wide wavelength range, while panel **c** shows an enlarged wavelength range across four CO lines. **d** and **e**: Spatially resolved spectrum obtained at the position B in the atmosphere shown in the same manner as in panels **b** and **c**. **f** and **g**: Spatially resolved spectrum obtained at the position C shown in the same manner as panels **b** and **c**. While the spatially resolved spectrum on the stellar disc (A) shows stronger absorption than the spatially unresolved spectrum, the spectra from the atmosphere (B and C) show the CO lines in prominent emission. Moreover, the emission lines at the position B are blueshifted with respect to the absorption lines in the spatially unresolved spectrum, while those at the position C are redshifted.

Figure 3: Velocity field map over the stellar disc and atmosphere of Antares. The velocity is estimated for the positions where the intensity is higher than 1.5% of the peak intensity. The black, ring-shaped gap corresponds to the limb of the star, where the velocity could not be measured. The reason is that the spatially resolved spectra on the limb show neither absorption nor emission because the absorption and emission cancel out due to the finite beam size (shown in the lower left corner). North is up, east is to the left.

## Methods

**Observations.** Our VLTI/AMBER observations took place on 2014 April 21, 22, 26, 27, and 28 (UTC), using four different Auxiliary Telescope (AT) array configurations—A1-C1-D0, A1-B2-C1, D0-H0-I1, and D0-G1-H0, as summarized in Extended Data Tables 1 and 2 (Program ID: 093.D-0468A/B, P.I.: K. Ohnaka). We used the high spectral resolution mode in the $K$ band (HR_K) with a spectral resolution of 12,000 (but binned down to 8,000 as described below) from 2.28 to 2.31 $\mu$m to observe the CO first overtones lines near the $v = 2 - 0$ band head at 2.294 $\mu$m. The extreme high brightness of $K = -4.1$ of Antares enabled us to detect fringes even on the very long baselines without using the VLTI fringe tracker FINITO (Antares is too bright for FINITO to work). The use of four different array configurations allowed us to extensively sample the object at projected baseline lengths from 4.6 to 82 m. Moreover, each night we observed Antares throughout the entire night to cover position angles as widely as possible. The extensive baseline length and position angle coverage resulted in a good $uv$ coverage as Extended Data Fig. 1 shows. The data sets taken on 2014 April 28 are of poor quality, and therefore, we had to discard most of them except for one data set. We observed $\alpha$ Cen A and $\alpha$ Cen B as interferometric calibrators for the compact configurations (A1-C1-D0 and A1-B2-C1) and extended configurations (D0-H0-I1 and D0-G1-H0), respectively. We adopted the angular diameters of $8.314 \pm 0.016$ mas and $5.856 \pm 0.027$ mas for $\alpha$ Cen A and $\alpha$ Cen B, respectively[30].

We reduced the data with amdlib 3.0.8, which is based on the P2VM algorithm[31,32]. It extracts three interferometric observables—visibility amplitude (or simply called visibility), closure phase, and differential phase—together with the (spatially unresolved) spectrum measured with each telescope. Although the original data were taken with a spectral resolution of 12,000, it turned out to be necessary to bin all the raw data (spectrally dispersed interferograms of the object, sky, dark, and P2VM calibration data) with a running box car function to gain S/N[11]. The data binned to a spectral resolution of 8,000 have S/N sufficient for the image reconstruction. We discarded the 20% frames with the poorest fringe S/N after checking different fringe selection criteria[11]. The wavelength calibration was carried out using the telluric lines. The uncertainty in the wavelength calibration is $1.7 \times 10^{-5}$ $\mu$m (2.2 km s$^{-1}$). The observed spectra of Antares were spectroscopically calibrated using that of $\alpha$ Cen A with the method described in our previous work[13].

**Limb-darkened disc fitting.** To estimate the angular size of Antares, we fitted the visibilities measured at each wavelength channel with a power-law-type limb-darkened disc[33]. Extended Data Figure 2 shows the derived limb-darkened (LD) disc angular diameter and the limb-darkening parameter $\alpha$ ($\alpha \rightarrow 0$ corresponds to a uniform disc) as a function of wavelength. The errors in the LD disc diameter and limb-darkening parameter were estimated with the bootstrap technique[34]. The mean limb-darkened disc diameter and limb-darkening parameter over the continuum channels are $37.61 \pm 0.12$ mas and $0.16 \pm 0.02$, respectively. The fit to the observed visibilities as a function of spatial frequency at three representative wavelengths (continuum, CO band head, and CO line centre) is shown in Extended Data Fig. 3. The data in the continuum are fairly fitted with the limb-darkened disc. However, the median reduced $\chi^2$ of the fit in the continuum is 11, which indicates the presence of inhomogeneities over the stellar disc. In the CO band head and CO lines, the limb-darkened disc diameter increases up to ~45 mas, and the limb-darkening parameter increases to $\sim 1$. However, the reduced $\chi^2$ of the fit in the CO band head and the CO lines is as large as 30, which means that the object appears far more complex than a limb-darkened disc.

**Image reconstruction.** We used the MiRA package ver.0.9.9[35] for the image reconstruction of Antares. We implemented the self-calibration imaging technique that takes advantage of differential phase measurements in addition to closure phases usually used in infrared interferometric image reconstruction[12,36]. In this technique, we first reconstruct the images at all continuum wavelength channels using the measured visibility amplitude and closure phase alone. On the one hand, the Fourier phase in the continuum can be computed from the reconstructed images at the continuum wavelength channels. On the other hand, differential phases measured with AMBER represent the phase in spectral lines with respect to the continuum. Therefore, we can restore the Fourier phase in the CO lines using the Fourier phase computed in the continuum and the differential phases measured in the CO lines. Then the image reconstruction is carried out at all wavelength channels using the measured visibility amplitudes and closure phases as well as the restored Fourier phases. The reconstructed images of Antares were convolved with a Gaussian point spread function (PSF) with a full width at half maximum of $5.1 \times 5.4$ mas, which was derived by fitting the central peak of the dirty beam.

As an initial model, we adopted a power-law-type limb-darkened disc with the angular diameter of $37.61$ mas and the limb-darkening parameter of $0.16$ as derived above. We used a Fermi-function-type prior $Pr(r) = 1/(\exp((r - r_{\rm p})/\varepsilon_{\rm p}) + 1)$, which was successfully used in our previous work[12,13]. This is a function of $r$ (radius in mas), and the parameter $r_{\rm p}$ defines the radius where the function rapidly decreases to 0. The parameter $\varepsilon_{\rm p}$ defines the steepness of the decrease. We set $r_{\rm p}$ and $\varepsilon_{\rm p}$ to be 22 mas and 1 mas, respectively. Combined with the maximum entropy regularization, this allows us to reconstruct the extended atmosphere without causing significant artifacts at very large distances from the star. We carried out the image reconstruction with different values for $r_{\rm p}$ and confirmed that the results are not noticeably affected up to $r_{\rm p}$ = 30 mas. Extended Data Figures 4 and 5 show comparison between the measured interferometric observables (visibility amplitude, Fourier phase, and closure phase) and those from the images reconstructed at eight wavelengths channels shown in Fig. 1.

We also carried out image reconstruction tests with simulated interferometric data generated from a limb-darkened disc with noise comparable to that of the Antares data. With the simulated image known, these experiments allow us to verify whether or not we can reconstruct the original image with the adopted reconstruction parameters and also to estimate the level of artifacts. We found out that the original limb-darkened disc image can be well reconstructed. The residuals after subtracting the original limb-darkened disc from the reconstructed image (both images convolved with the aforementioned Gaussian PSF) are 1.5%. This also means that the weak, central spot with the intensity contrast of 3–4% seen in the continuum images (Figs. 1a and 1e) is partially due to the reconstruction artifact but may also partially show a real structure. The deviations of the observed visibilities from the limb-darkened disc as mentioned in the previous section also indicate the presence of inhomogeneities in the continuum images. We note that other structures seen in the CO line images are stronger than this weak, central spot seen in the continuum images.

To extract the spatially resolved spectrum at each position over the stellar disc and the atmosphere, we normalised the reconstructed image (convolved with the Gaussian PSF) at each wavelength channel so that the flux integrated over the entire reconstructed image is equal to the flux observed at the corresponding wavelength with AMBER.

**Code availability** The AMBER data reduction package is available at http://www.jmmc.fr/data_processing_amber.htm. The image reconstruction package MiRA is available at http://cral.univ-lyon1.fr/labo/perso/eric.thiebaut/?Software/MiRA. We have opted not to make the code for the self-calibration image reconstruction and the analysis of the reconstructed images available. The reason is that the routines are customized for the present analysis and cannot be readily applied to other cases.

**Source data availability** The data sets generated and analysed during this study are available from the corresponding author upon reasonable request.

30. Kervella, P. et al. The diameters of $\alpha$ Centauri A and B. A comparison of the asteroseismic and VINCI/VLTI views. Astron. Astrophys., **404**, 1087-1097 (2003)

31. Tatulli, E. et al. Interferometric data reduction with AMBER/VLTI. Principle, estimators, and illustration. Astron. Astrophys., **464**, 29-42 (2007)

32. Chelli, A. et al. Optimised data reduction for the AMBER/VLTI instrument. Astron. Astrophys., **502**, 705-709 (2009)

33. Hestroffer, D. Centre to limb darkening of stars. New model and application to stellar interferometry. Astron. Astrophys., **327**, 199-206 (1997)

34. Efron, B., & Tibshirani, R. J. An Introduction to the Bootstrap, Chapman & Hall, New York (1993)

35. Thiébaut, E. MIRA: an effective imaging algorithm for optical interferometry. SPIE Proceedings, **7013**, 70131I (2008)

36. Millour, F. et al. Imaging the spinning gas and dust in the disc around the supergiant A[e] star HD 62623. Astron. Astrophys., **526**, A107

Extended Data Table 1: Summary of VLTI/AMBER observations of Antares with the A1-B2-C1-D0 AT quadruplet. $B_{\mathrm{p}}$: Projected baseline length. PA: Position angle of the baseline vector projected onto the sky. $s$: Seeing in the visible. $\tau_0$: Coherence time in the visible. DIT: Detector Integration Time. $N_{\mathrm{f}}$: Number of frames in each exposure. $N_{\mathrm{exp}}$: Number of exposures.

| # | $t_{\mathrm{obs}}$ | $B_{\mathrm{p}}$ | PA | $s$ | $\tau_0$ | DIT $\times N_{\mathrm{f}} \times N_{\mathrm{exp}}$ |
|---|---|---|---|---|---|---|
| | (UTC) | (m) | (°) | ($''$) | (ms) | (ms) |
| 2014 Apr 21 (UTC) A1-C1-D0 | | | | | | |
| 1 | 02:43:09 | 11.52/22.43/32.90 | 20/−10/0 | 1.5 | 1.9 | 120 × 500 × 5 |
| 2 | 03:21:34 | 12.23/22.37/33.06 | 31/−5/ 7 | 1.2 | 2.4 | 120 × 500 × 5 |
| 3 | 04:04:05 | 13.20/22.36/33.53 | 42/ 2/17 | 0.99 | 2.8 | 120 × 500 × 5 |
| 4 | 04:41:50 | 14.09/22.40/34.12 | 50/ 7/24 | 0.8 | 3.4 | 120 × 500 × 5 |
| 5 | 05:23:12 | 14.95/22.48/34.83 | 57/13/31 | – | 2.4 | 120 × 500 × 5 |
| 6 | 06:03:10 | 15.58/22.57/35.40 | 63/1836 | 1.8 | 1.5 | 120 × 500 × 5 |
| 7 | 06:47:01 | 15.95/22.62/35.75 | 69/24/42 | 1.7 | 1.6 | 120 × 500 × 5 |
| 8 | 08:09:17 | 15.57/22.41/35.13 | 77/32/50 | 1.7 | 1.6 | 120 × 500 × 3 |
| 9 | 08:46:55 | 14.83/22.06/34.04 | 81/35/53 | 0.9 | 3.1 | 120 × 500 × 5 |
| 10 | 09:24:00 | 13.82/21.55/32.51 | 85/37/55 | 0.9 | 3.1 | 120 × 500 × 5 |
| 11 | 10:00:53 | 12.52/20.85/30.48 | 88/39/57 | 0.6 | 4.5 | 120 × 500 × 5 |
| 2014 Apr 22 (UTC) A1-B2-C1 | | | | | | |
| 12 | 02:08:58 | 4.76/11.24/11.16 | 89/−14/11 | 0.7 | 6.8 | 120 × 500 × 5 |
| 13 | 02:45:32 | 6.10/11.20/11.58 | 93/ −9/22 | 1.0 | 4.8 | 120 × 500 × 5 |
| 14 | 03:25:27 | 7.57/11.17/12.40 | 96/ −3/34 | 1.3 | 3.9 | 120 × 500 × 5 |
| 15 | 04:01:35 | 8.67/11.17/13.23 | 99/ 2/43 | 0.8 | 6.5 | 120 × 500 × 5 |
| 16 | 04:38:12 | 9.60/11.19/14.09 | 102/ 7/50 | 0.7 | 6.7 | 120 × 500 × 5 |
| 17 | 05:14:31 | 10.33/11.22/14.86 | 105/12/56 | 0.8 | 6.5 | 120 × 500 × 5 |
| 18 | 05:51:06 | 10.86/11.26/15.47 | 109/17/62 | 0.9 | 5.2 | 120 × 500 × 5 |
| 19 | 06:31:22 | 11.18/11.29/15.86 | 112/22/67 | 0.7 | 7.5 | 120 × 500 × 5 |
| 20 | 07:24:18 | 11.29/11.28/15.93 | 118/28/73 | 0.6 | 7.9 | 120 × 500 × 5 |
| 21 | 08:01:10 | 11.12/11.20/15.60 | 123/31/77 | 0.6 | 8.3 | 120 × 500 × 5 |
| 22 | 08:37:20 | 10.82/11.05/14.96 | 128/34/80 | 0.7 | 6.4 | 120 × 500 × 5 |
| 23 | 09:18:48 | 10.34/10.77/13.86 | 135/37/85 | 0.7 | 7.0 | 120 × 500 × 5 |
| 24 | 09:57:29 | 9.83/10.41/12.50 | 143/39/89 | 0.7 | 6.5 | 120 × 500 × 5 |

Extended Data Table 2: Summary of VLTI/AMBER observations of Antares with the D0-G1-H0-I1 AT quadruplet given in the same manner as in Extended Data Table 1.

| # | $t_{\rm obs}$ (UTC) | $B_{\rm p}$ (m) | PA (°) | $s$ ($''$) | $\tau_0$ (ms) | DIT $\times N_{\rm f} \times N_{\rm exp}$ (ms) |
|---|---|---|---|---|---|---|
| 2014 Apr 26 (UTC) D0-H0-I1 | | | | | | |
| 25 | 02:07:28 | 45.23/30.34/39.01 | 15/137/57 | 0.9 | 2.1 | $120 \times 500 \times 5$ |
| 26 | 03:15:02 | 50.09/34.77/55.17 | 35/136/73 | 1.1 | 1.9 | $120 \times 500 \times 5$ |
| 27 | 04:00:06 | 54.32/37.08/64.82 | 46/137/81 | 0.8 | 2.4 | $120 \times 500 \times 5$ |
| 28 | 04:47:06 | 58.55/38.87/72.98 | 55/140/87 | 1.3 | 1.6 | $120 \times 500 \times 5$ |
| 29 | 05:37:14 | 62.03/40.08/79.01 | 62/143/92 | 1.0 | 1.8 | $120 \times 500 \times 5$ |
| 30 | 06:21:11 | 63.72/40.62/81.80 | 68/147/97 | 1.4 | 1.4 | $120 \times 500 \times 5$ |
| 31 | 07:26:46 | 63.26/40.73/81.54 | 75/154/104 | 0.9 | 2.0 | $120 \times 500 \times 5$ |
| 32 | 08:11:46 | 60.67/40.51/78.48 | 80/160/110 | 0.9 | 2.1 | $120 \times 500 \times 5$ |
| 33 | 08:59:08 | 55.93/40.21/73.13 | 84/166/117 | 0.7 | 2.7 | $120 \times 500 \times 5$ |
| 2014 Apr 27 (UTC) D0-G1-H0 | | | | | | |
| 34 | 02:29:16 | 46.72/70.90/47.76 | 23/162/121 | 1.1 | 2.0 | $120 \times 500 \times 5$ |
| 35 | 03:12:45 | 50.23/71.28/55.02 | 36/165/121 | 1.1 | 2.0 | $120 \times 500 \times 5$ |
| 36 | 03:54:32 | 54.17/71.45/60.87 | 45/169/122 | 0.7 | 3.0 | $120 \times 500 \times 5$ |
| 37 | 04:34:12 | 57.79/71.51/65.24 | 53/174/124 | 1.1 | 2.0 | $120 \times 500 \times 5$ |
| 38 | 05:16:01 | 60.99/71.53/68.58 | 60/178/126 | 1.2 | 2.0 | $120 \times 500 \times 5$ |
| 39 | 06:01:12 | 63.28/71.53/70.74 | $66/-177/130$ | 0.8 | 3.1 | $120 \times 500 \times 5$ |
| 40 | 06:45:19 | 63.99/71.50/71.52 | $71/-172/134$ | 1.1 | 2.1 | $120 \times 500 \times 5$ |
| 41 | 07:29:46 | 62.98/71.40/71.20 | $76/-167/140$ | 0.9 | 2.5 | $120 \times 500 \times 5$ |
| 42 | 08:13:0 | 60.24/71.16/70.11 | $80/-163/146$ | 1.0 | 2.2 | $120 \times 500 \times 5$ |
| 2014 Apr 28 (UTC) D0-H0-I1 | | | | | | |
| 43 | 10:07:18 | 44.75/39.91/62.09 | 92/178/132 | 0.9 | 2.0 | $120 \times 500 \times 3$ |

Extended Data Figure 1: The $uv$ coverage of our VLTI/AMBER observations with four different AT configurations.

Extended Data Figure 2: Limb-darkened disc fit to the AMBER data of Antares. **a:** Power-law-type limb-darkened disc diameter as a function of wavelength (red dots). The scaled, observed spectrum is shown in black. **b:** Limb-darkening parameter as a function of wavelength. In both panels, the error bars represent $1\sigma$.

Extended Data Figure 3: Limb-darkened disc fit to the observed visibilities as a function of spatial frequency. The fit at a wavelength channel in the continuum, in the CO band head, and at the center of one of the CO lines is shown in panels (**a** and **b**), (**c** and **d**), and (**e** and **f**), respectively. The observed visibilities are plotted with the dots with the $1\sigma$ errors computed over $N_{\rm f} \times N_{\rm exp}$ frames as listed in Extended Data Tables 1 and 2. The limb-darkened disc fit is shown with the curves.

Extended Data Figure 4: Comparison between the measured interferometric observables and those from the images reconstructed near the CO band head. The filled circles in the top row (**a–d**) show the wavelength channels in the observed spectrum, which correspond to the wavelengths of the images shown in Figs. 1a–1d. The second, third, fourth, and fifth rows show a comparison for the visibility at spatial frequencies lower than 55 arcsec$^{-1}$, visibility at spatial frequencies higher than 55 arcsec$^{-1}$, Fourier phase, and closure phase, respectively. In these panels, the observed data are plotted by the red dots with the error bars ($1\sigma$ as described in the legend of Fig. 3). The blue triangles represent the values from the image reconstruction. The reduced $\chi^2_{\rm red}$ values including the visibilities, Fourier phases, and closure phases, are given in the panels in the bottom row.

Extended Data Figure 5: Comparison between the measured interferometric observables and those from the images reconstructed across one of the CO lines. The panels are shown in the same manner as Extended Data Fig. 4. The filled circles in the top row (**a**–**d**) show the wavelength channels in the observed spectrum, which correspond to the wavelengths of the images shown in Figs. 1e–1h.

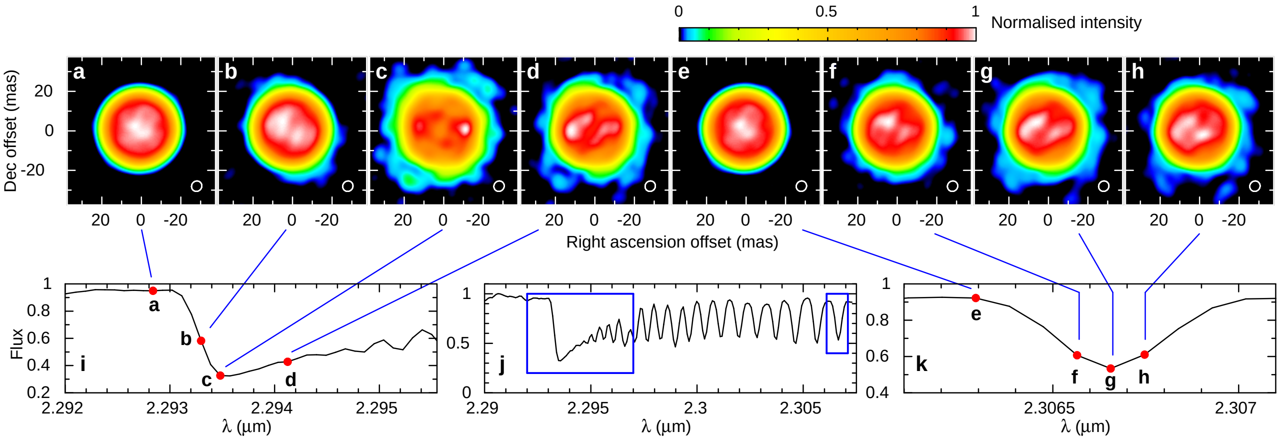
0
0.5
1
Normalised intensity
a
b
c
d
e
f
g
h
Dec offset (mas)
20
0
-20
Right ascension offset (mas)
Flux
i
j
k
λ (μm)
2.292
2.293
2.294
2.295
2.29
2.295
2.3
2.305
2.3065
2.307
1
0.8
0.6
0.4
0.2
0.5

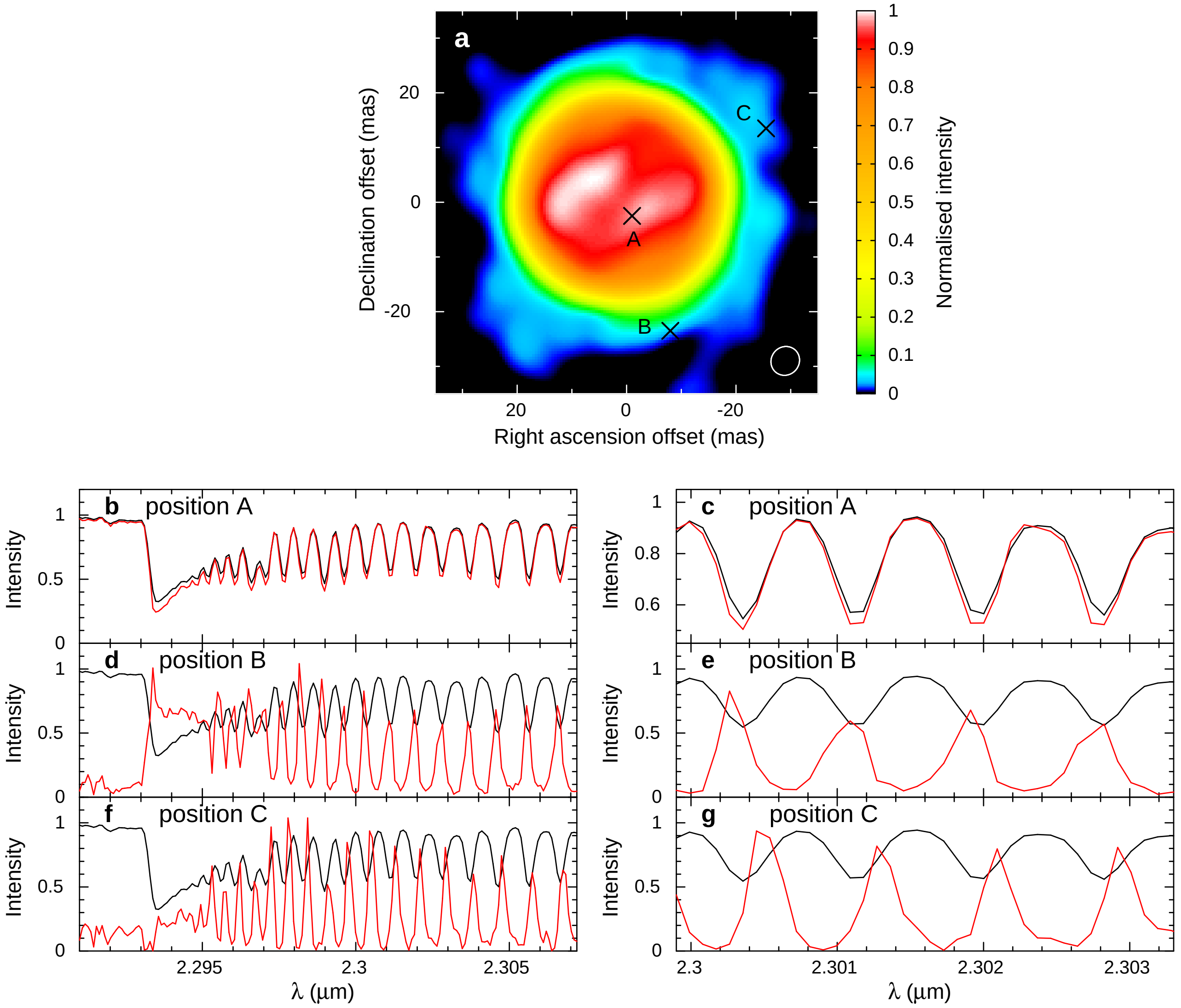
a
A
B
C
Declination offset (mas)
Right ascension offset (mas)
20
0
-20
Normalised intensity
1
0.9
0.8
0.7
0.6
0.5
0.4
0.3
0.2
0.1
0
b position A
c position A
d position B
e position B
f position C
g position C
Intensity
0
0.5
1
0.6
0.8
2.295
2.3
2.305
2.301
2.302
2.303
λ (μm)

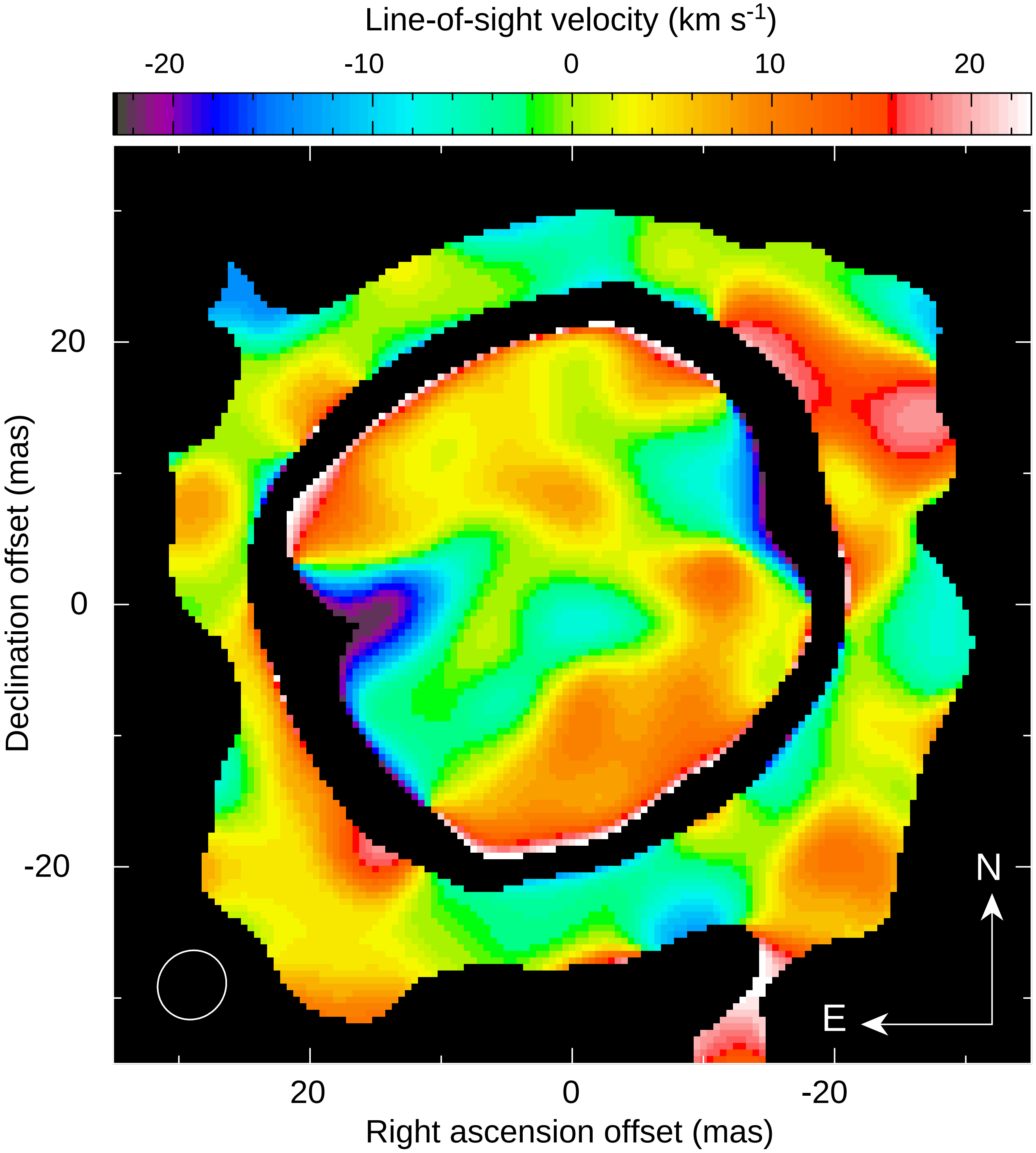
Line-of-sight velocity (km s$^{-1}$)
-20
-10
0
10
20
Declination offset (mas)
20
0
-20
Right ascension offset (mas)
20
0
-20
N
E

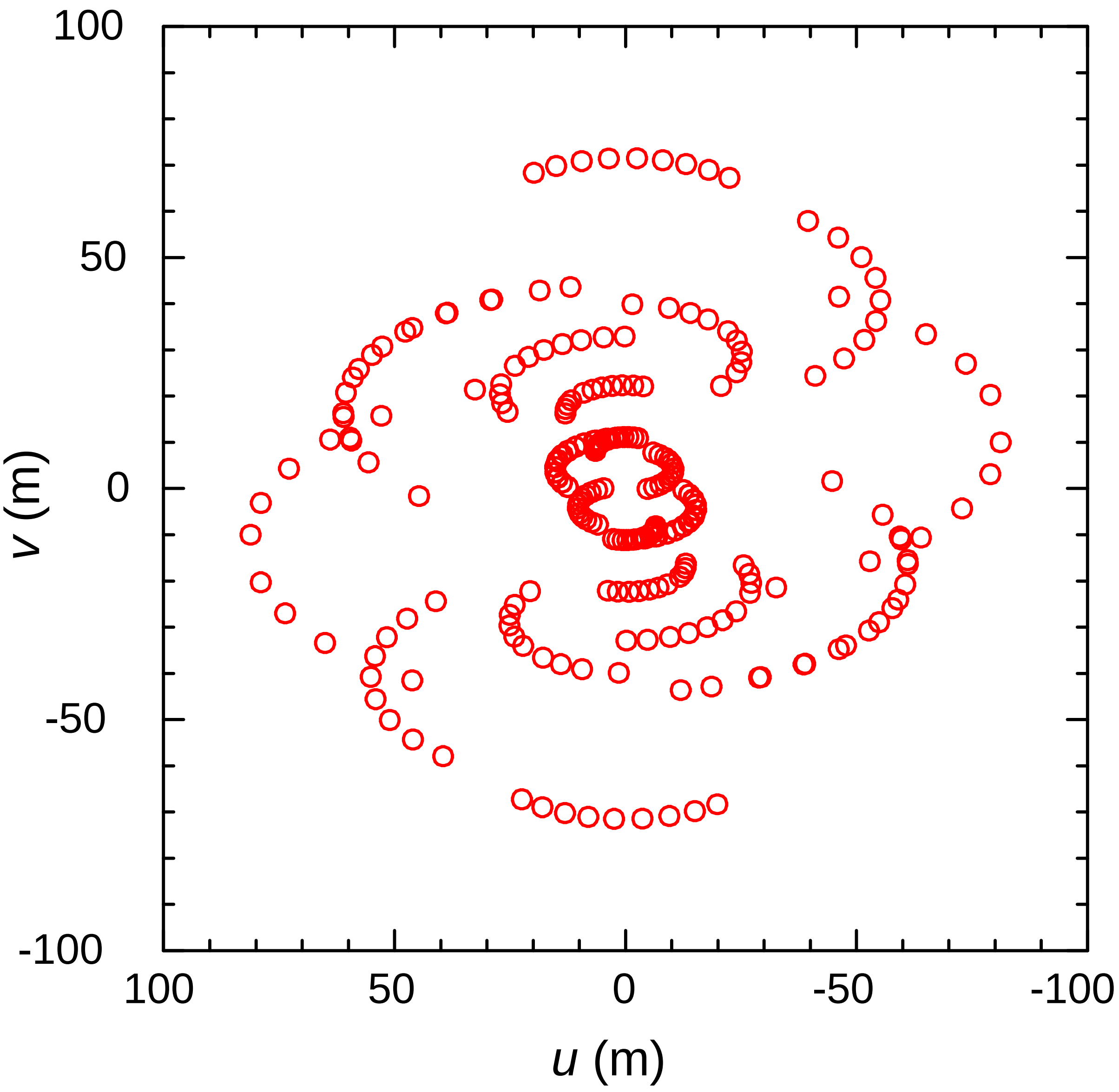
100
50
0
-50
-100
100
50
0
-50
-100
v (m)
u (m)

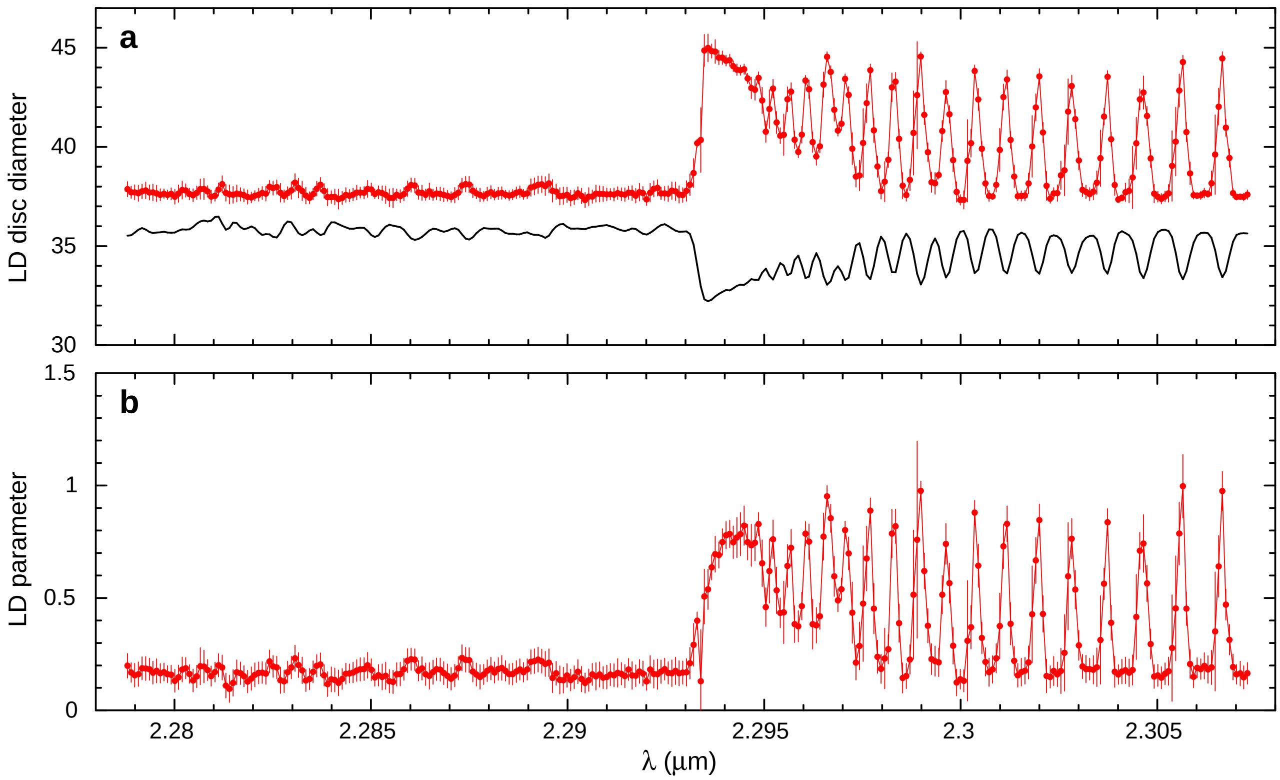
a
b
LD disc diameter
45
40
35
30
LD parameter
1.5
1
0.5
0
2.28
2.285
2.29
2.295
2.3
2.305
λ (μm)

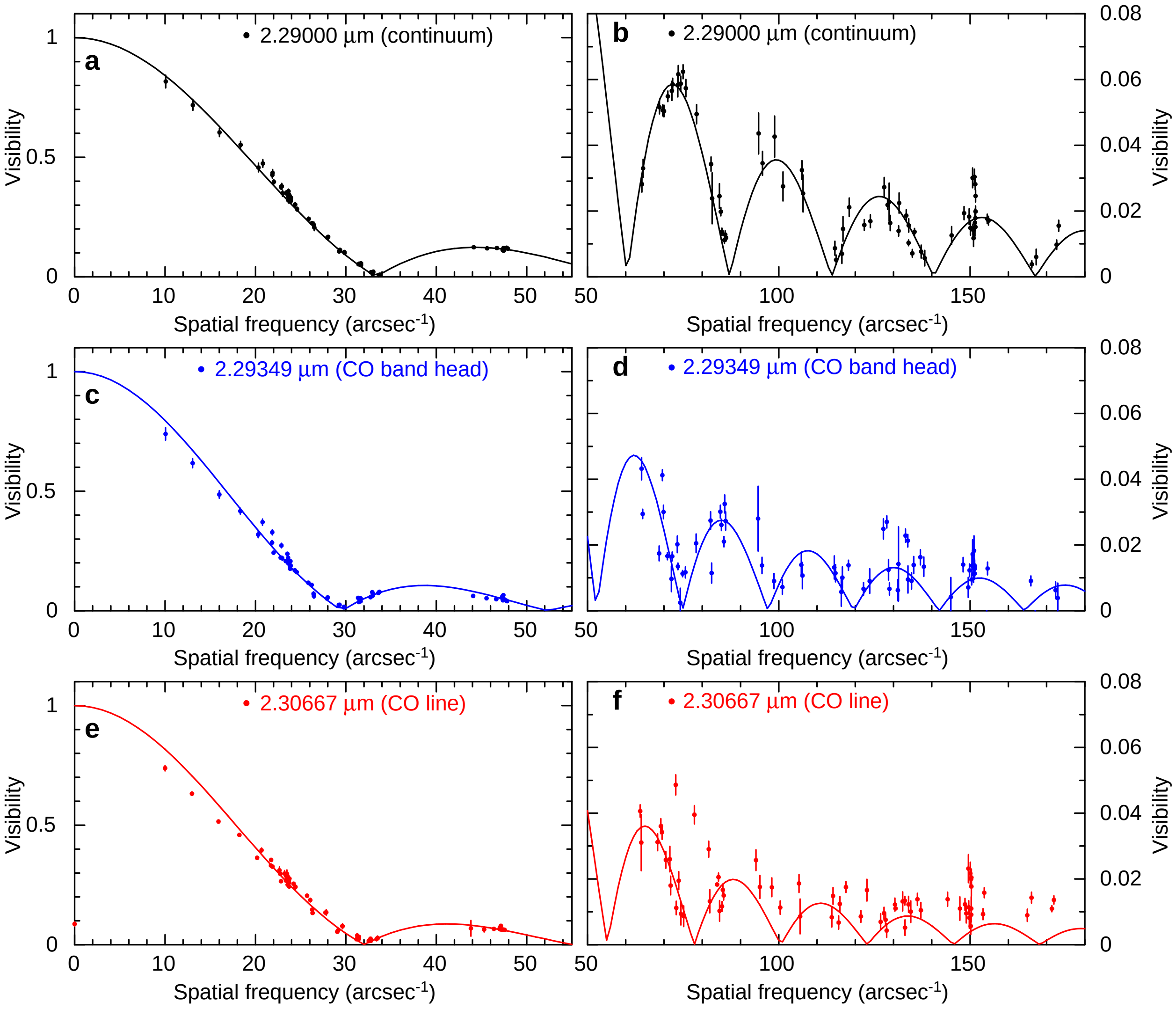
a
• 2.29000 µm (continuum)
b
• 2.29000 µm (continuum)
c
• 2.29349 µm (CO band head)
d
• 2.29349 µm (CO band head)
e
• 2.30667 µm (CO line)
f
• 2.30667 µm (CO line)
Visibility
0
0.5
1
0.08
0.06
0.04
0.02
0
0
10
20
30
40
50
100
150
Spatial frequency (arcsec$^{-1}$)

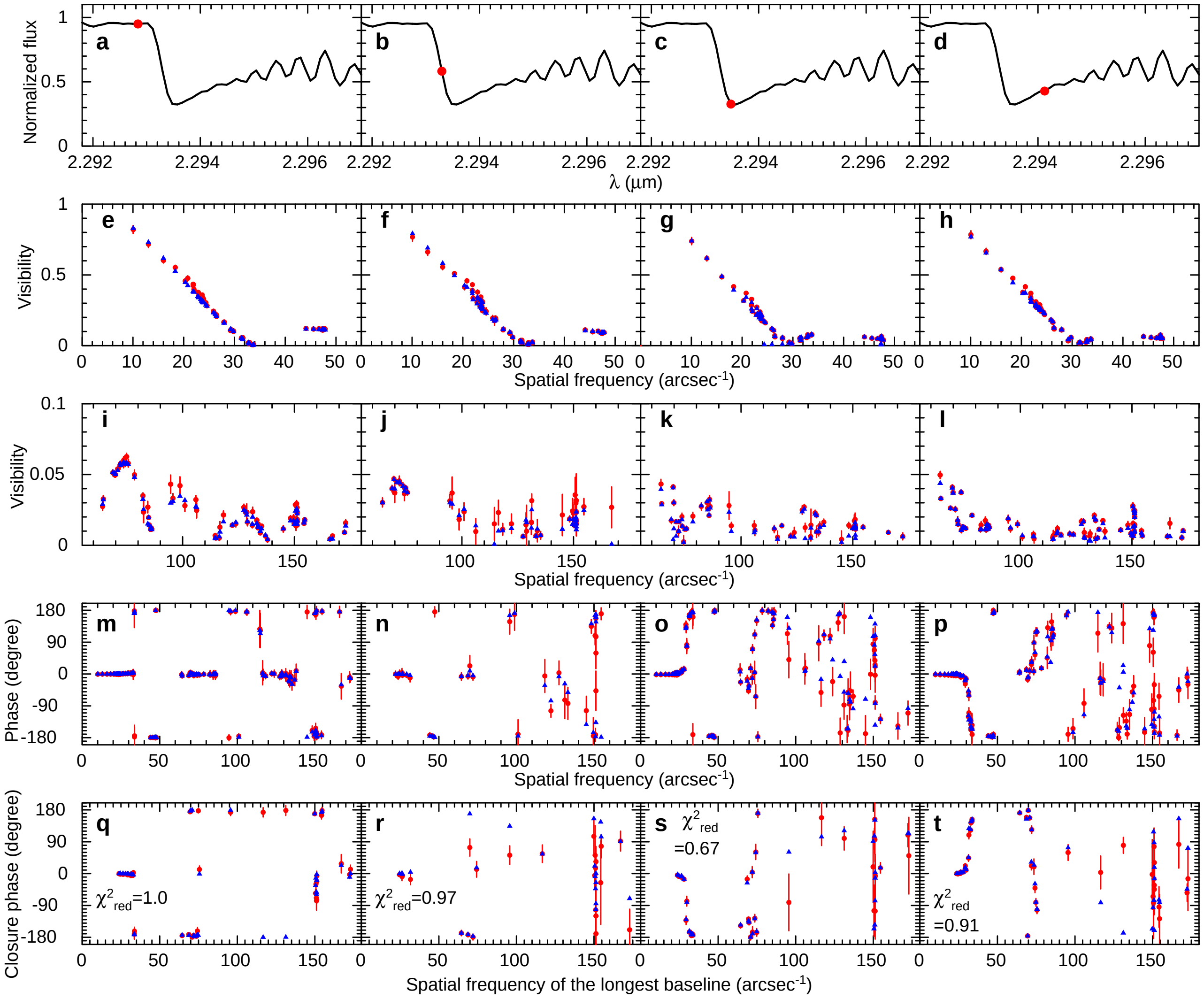
Normalized flux
1
0.5
0
a
b
c
d
2.292
2.294
2.296
λ (μm)
Visibility
1
0.5
0
e
f
g
h
0
10
20
30
40
50
Spatial frequency (arcsec$^{-1}$)
Visibility
0.1
0.05
0
i
j
k
l
100
150
Spatial frequency (arcsec$^{-1}$)
Phase (degree)
180
90
0
-90
-180
m
n
o
p
0
50
100
150
Spatial frequency (arcsec$^{-1}$)
Closure phase (degree)
180
90
0
-90
-180
q
r
s
t
$\chi^2_{red}$=1.0
$\chi^2_{red}$=0.97
$\chi^2_{red}$ =0.67
$\chi^2_{red}$ =0.91
0
50
100
150
Spatial frequency of the longest baseline (arcsec$^{-1}$)

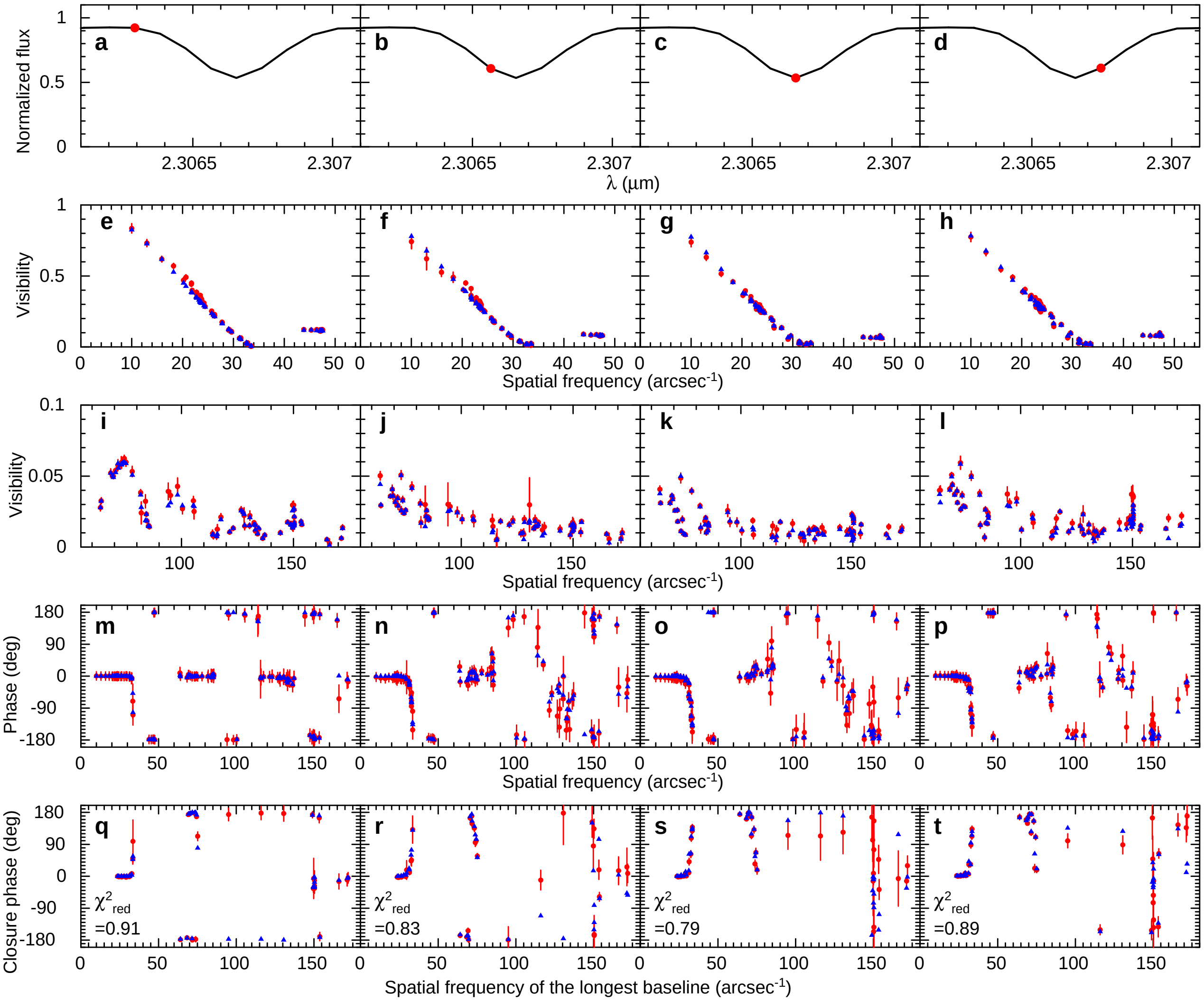
a
b
c
d
Normalized flux
1
0.5
0
2.3065
2.307
λ (μm)
e
f
g
h
Visibility
Spatial frequency (arcsec-1)
i
j
k
l
0.1
0.05
m
n
o
p
Phase (deg)
180
90
-90
-180
q
r
s
t
Closure phase (deg)
χ2red =0.91
χ2red =0.83
χ2red =0.79
χ2red =0.89
Spatial frequency of the longest baseline (arcsec-1)